AFRL-VS-HA-TR-2005-1106

Dynamically Resolved Simulation of Atmospheric Features and Turbulence Using Advanced Models and Adaptive Algorithms

D. Scott McRae
Xudong Xiao
Hassan A. Hassan

North Carolina State University
Department of Mechanical and Aerospace Engineering
P.O. Box 7910
Raleigh, NC 27695-7910

16 February 2005

Scientific Report No. 1

AIR FORCE RESEARCH LABORATORY
Space Vehicles Directorate
29 Randolph Rd
AIR FORCE MATERIEL COMMAND
Hanscom AFB, MA 01731-3010

This technical report has been reviewed and is approved for publication.

AFRL-VS-HA-TR-2005-1106

/signed/

GEORGE Y. JUMPER
Contract Manager

/signed/

ROBERT BELAND, Chief
Battlespace Surveillance Innovation Center

This report has been reviewed by the ESC Public Affairs Office (PA) and is releasable to the National Technical Information Service (NTIS).

Qualified requestors may obtain additional copies from the Defense Technical Information Center (DTIC). All others should apply to the National Technical Information Service.

If your address has changed, if you wish to be removed from the mailing list, or if the addressee is no longer employed by your organization, please notify AFRL/VSIM, 29 Randolph Rd., Hanscom AFB, MA 01731-3010. This will assist us in maintaining a current mailing list.

Do not return copies of this report unless contractual obligations or notices on a specific document require that it be returned.

Using Government drawings, specifications, or other data included in this document for any purpose other than Government procurement does not in any way obligate the U.S. Government. The fact that the Government formulated or supplied the drawings, specifications, or other data does not license the holder or any other person or corporation; or convey any rights or permission to manufacture, use, or sell any patented invention that may relate to them.

This report is published in the interest of scientific and technical information exchange and its publication does not constitute the Government's approval or disapproval of its ideas or findings.

REPORT DOCUMENTATION PAGE

Form Approved
OMB No. 0704-0188

1. REPORT DATE *(DD-MM-YYYY)*	2. REPORT TYPE	3. DATES COVERED *(From - To)*
16 Feb 2005	Scientific Report No. 1	17 Jun 2004 - 16 Feb 2005

4. TITLE AND SUBTITLE
Dynamically Resolved Simulation of Atmospheric Features and Turbulence Using Advanced Models and Adaptive Algorithms

5a. CONTRACT NUMBER
FA8718-04-C-0019

5b. GRANT NUMBER

5c. PROGRAM ELEMENT NUMBER

6. AUTHOR(S)
D. Scott McRae, Xudong Xiao, Hassan A. Hassan

5d. PROJECT NUMBER
1010

5e. TASK NUMBER
01

5f. WORK UNIT NUMBER
A1

7. PERFORMING ORGANIZATION NAME(S) AND ADDRESS(ES)
North Carolina State University
Dept. of Mechanical and Aerospace Engineering
Raleigh, NC 27695-7910

8. PERFORMING ORGANIZATION REPORT NUMBER

9. SPONSORING/MONITORING AGENCY NAME(S) AND ADDRESS(ES)
Air Force Research Laboratory
29 Randolph Road
Hanscom AFB, MA 01731-3010

10. SPONSOR/MONITOR'S ACRONYM(S)
AFRL/VSBYA

11. SPONSOR/MONITOR'S REPORT NUMBER(S)
AFRL-VS-HA-TR-2005-1106

12. DISTRIBUTION/AVAILABILITY STATEMENT
Approved for public release; distribution unlimited.

13. SUPPLEMENTARY NOTES

14. ABSTRACT
Development of the North Carolina State University (NCSU) adaptive high-resolution atmospheric model and the atmospheric version of the NCSU k-ζ turbulence model continued during this contract period. The boundary condition implementation at the lateral boundaries was changed to radiative type to better preserve fixed condition boundary values. A sponge layer condition was installed at the upper boundary. The solution redistribution algorithm after mesh adaptation was changed to a weighted essentially non-oscillatory algorithm in order to improve accuracy. Basic development of the turbulence modsel was completed and the equations are included herein. The full turbulence model was included in the code and 3-D runs were initiated to begin comparison with observation and other codes. A widely used generic 2-D windstorm case was used for confirmation and verification of the changes. Initial results demonstrated the breakdown of shear layers into clear air turbulence of sufficient severity to produce 1-g vertical accelerations for aircraft.

15. SUBJECT TERMS
Optical turbulence, Atmospheric model, MM5, Turbulence model, Adaptive mesh

16. SECURITY CLASSIFICATION OF:			17. LIMITATION OF ABSTRACT	18. NUMBER OF PAGES	19a. NAME OF RESPONSIBLE PERSON
a. REPORT	b. ABSTRACT	c. THIS PAGE			George Y. Jumper
Unclassified	Unclassified	Unclassified	UU	26	19b. TELEPHONE NUMBER *(Include area code)* 781-377-3148

Table of Contents

FIGURES

1. INTRODUCTION

Predicting the propagation of optical frequency beams through the atmosphere depends greatly on knowledge of the detailed state of the atmosphere along the propagation path. This statement is appropriate regardless of the altitude at which the propagation is examined. Two atmospheric characteristics that directly impede beam transmission are optical scale turbulence and the presence of clouds due to gravity waves and other generation processes. It has also been observed that gravity wave instability processes can lead to local turbulence production. However, this is one of the "–least quantified aspects of gravity wave forcing of the middle atmosphere at present," as noted by Fritts and Alexander in a recent review article [1].

In the case of optical turbulence, considerable experimental effort has been expended toward expanding the data base of temperature fluctuations in the atmosphere, with accepted average profiles having been obtained for selected important locales as noted in Reference 2 which provides an excellent assessment of past work and the issues. Unfortunately, measuring directly the detailed state of the atmosphere is not usually possible or practical for a significant range of conditions, locations and times, especially given terrain and local condition influences. This situation points to the need for simulation/modeling tools that could be used to predict, based on inputs of terrain and local conditions, local levels of optical turbulence. However, the presently available atmospheric modeling tools do not provide a means of simulating directly the scales needed to assess local optical turbulence, due to resolution and other issues.

This research project was initiated to continue development of a high resolution meso-scale atmospheric model, based on the well developed model MM5 [3], to provide dynamic resolution of selected features and characteristics of the atmosphere simulation. The goal is to provide a very high resolution prediction of optical turbulence parameters. The remainder of this report will review the code development and improvements performed during the first year of the contract period followed by a review of the results obtained to date. Relevant details of the following activity will be included:

1) Installation of improved boundary condition implementations for use when the adaptive algorithm is used for the entire mesoscale domain. This permits adaptation to be used instead of nesting to increase resolution. This implementation will also provide improved one way nest boundary conditions.

2) Further checkout of the transformation coding was performed.

3) A new method was installed for redistribution of the solution after adaptation of the mesh.

4) Basic development of the atmospheric version of the NCSU k-ζ turbulence model was completed during this period. The fully developed version was installed in the updated code.

A 2-D case consisting of sounding data from a Colorado windstorm event applied to a domain containing a generic mountain [4] was used for code development. Many other models have been executed for this case and the strong shear coupled with the generic mountain topography provides conditions usually leading to gravity waves and turbulence. Standard confirmation steps for the adaptive mesh algorithm were performed using this case. Currently, 3-D runs are in progress to compare the results of the high-resolution mesoscale model and turbulence model with data and other atmospheric models.

2. DYNAMICALLY RESOLVED MESOSCALE MODEL-MODIFICATIONS TO MM5

The code structure and physical modeling in MM5 [3] is retained. A 3-D grid domain (nest) is imbedded in the inner MM5 nest with increased mesh node density and with the NCSU dynamic solution adaptive mesh algorithm DSAGA [5-7] applied to further increase resolution where needed. The flow in this imbedded region is solved, to LES scales, with the standard non-hydrostatic equations transformed to a general time-varying structured grid. DSAGA uses r-refinement adaptation to resolve automatically selected scales and features in the solution. The goal of the adaptation is to provide LES-scale resolution for the developing turbulence. This capability will also allow resolution of the dynamic processes from gravity wave generation to break-down. This adaptive algorithm is developed sufficiently such that any criteria or linear combination of criteria may be used to promote grid clustering, thereby insuring resolution of the features from which the criteria are derived. Within the dynamically resolved nest, an extension of $k-\zeta$ (enstrophy, or variance of vorticity) turbulence model [8, 9] is used to provide LES sub-grid scale turbulence modeling. This model includes fundamental flow physics and has proved to be superior to standard models when used in modeling turbulence.

The outer MM5 and imbedded high-resolution fields are executed alternately. After each iteration on the outer MM5 domain, the boundary values and tendencies for the imbedded mesh are interpolated from the outer MM5 domain. Temporal accuracy is preserved by advancing the solution in the imbedded domain to the same time level as the outer domain. This procedure is the same as MM5, but the time step in the imbedded domain may vary due to the grid adaptation.

3. TRANSFORMATION OF GOVERNING EQUATIONS

In order to install the dynamic adaptive mesh algorithm in MM5, the non-hydrostatic governing equations were transformed to a time-varying curvilinear coordinate system that is coincident with either of the outer domain, a nest boundary, or a portion of the standard nest. The transformation is Galilean invariant, implying mathematically that the solution to the governing equations is not changed by the mesh adjustment to improve solution resolution.

The equations, initially defined in the x, y, σ coordinate system, are transformed using the chain-rule in all three dimensions to a uniform computational coordinate system, according to:

$$\tau = t$$
$$\xi_i = \xi_i(x, y, z, \sigma)$$

where σ is the non-dimensional pressure coordinate. The resulting equations read

$$\frac{\partial \mathrm{U}}{\partial t} + \frac{\partial \mathrm{U}}{\partial \xi_i}\frac{\partial \xi_i}{\partial t} + m^2 \frac{\partial \mathrm{E}}{\partial \xi_i}\frac{\partial \xi_i}{\partial x} + m^2 \frac{\partial \mathrm{E}}{\partial \xi_i}\frac{\partial \xi_i}{\partial y} + \frac{\partial \mathrm{G}}{\partial \xi_i}\frac{\partial \xi_i}{\partial \sigma} = \mathrm{S}$$

where

$$\mathrm{U} = [p^* p', p^* u, p^* v, p^* w, p^* T]^T$$
$$\mathrm{E} = \frac{u}{m}[p^* p', p^* u, p^* v, p^* w, p^* T]^T$$
$$\mathrm{F} = \frac{v}{m}[p^* p', p^* u, p^* v, p^* w, p^* T]^T$$
$$\mathrm{G} = \dot{\sigma}[p^* p', p^* u, p^* v, p^* w, p^* T]^T$$

m is the map scale, p^* the reference pressure, and p' the pressure perturbation, T the temperature, and u, v and w are velocity components in the x-, y- and z-direction, respectively. All other terms, such as pressure gradient, Coriolis force, and gravity terms, are included in **S**, c.f. Reference 3 for more detail. The above equations are discretized in the Arakawa-B [10] type staggered grid, using the same finite difference stencils as MM5, e.g., the stencils used in the x-direction in MM5 are applied to ξ_1 direction here. These equations are also solved using the leap-frog scheme. In order to obtain accurate discretization in the curvilinear staggered grid, three sets of metric derivatives are calculated to be consistent to the differencing of flow variables. The variables and metric derivatives are defined at three different locations as shown in Figure 1, i.e., the cell center (cross, for p' and T), the center of cell edges (dot, for u and v) and the center of ξ_3 = const cell surface (Δ, for w and σ).

4. MODIFICATION OF THE SEMI-IMPLICIT SCHEME

In MM5, in order to remove the limitation on the time step due to small mesh spacing in the vertical direction, the following two coupled equations for w and p' are solved implicitly:

$$\frac{\partial w}{\partial t} - \frac{\rho_0 g}{\rho p^*}\frac{\partial p'}{\partial \sigma} + \frac{g}{\gamma}\frac{p'}{p} = S_w$$
$$\frac{\partial p'}{\partial t} - \frac{\rho_0 g \gamma p}{p^*}\frac{\partial w}{\partial \sigma} - \rho_0 g w = S_{p'}$$

This results in a tridiagonal system along the σ-direction for w' in the uniform mesh, which can be solved directly. But in the adaptive mesh, the σ variation is transformed, therefore, this set must be solved iteratively. The iteration scheme chosen is as follows:

1) Initialize as:

$$p'^{(0)} = p'^{t}, w^{(0)} = w^{t}$$

2) Then solve iteratively:

$$\frac{w^{(i+1)} - w^{t}}{\Delta t} - \frac{\rho_0 g}{\rho p^*}\left(\frac{\partial p'}{\partial \xi_3}\right)^{(i+1)} \xi_{3,\sigma} + \frac{g}{\gamma}\frac{p'^{(i+1)}}{p} = S_w + \frac{\rho_0 g}{\rho p^*}\left[\left(\frac{\partial p'}{\partial \xi_1}\right)^{(i)} \xi_{1,\sigma} + \left(\frac{\partial p'}{\partial \xi_2}\right)^{(i)} \xi_{2,\sigma}\right]$$

$$\frac{p'^{(i+1)} - p'^{t}}{\Delta t} - \frac{\rho_0 g \gamma p}{p^*}\left(\frac{\partial p'}{\partial \xi_3}\right)^{(i+1)} \xi_{3,\sigma} - \rho_0 g w^{(i+1)} = S_{p'} + \frac{\rho_0 g \gamma p}{p^*}\left[\left(\frac{\partial p'}{\partial \xi_1}\right)^{(i)} \xi_{1,\sigma} + \left(\frac{\partial p'}{\partial \xi_2}\right)^{(i)} \xi_{2,\sigma}\right]$$

3) When converged,

$$p'^{t+1} = p'^{(i+1)}, w^{t+1} = w^{(i+1)}$$

5. ADAPTIVE GRID ALGORITHM

In the current implementation of the adaptive algorithm, the integration proceeds in two steps; the first is the integration of the governing equations on the mesh adapted to the solution at the previous time step. After this integration is completed, the mesh is adapted to this new solution and the invariant solution is redistributed over the new mesh. The weight function that controls the adaptation is based on the magnitude of local vorticity and is processed and smoothed to influence the relative adaptation of the grid and the smoothness of the grid metric derivative distribution. The redistribution step is equivalent to an advection of the invariant solution and is thereby important to the accuracy of the integration. In order to improve the accuracy of this step, a fifth order weighted essentially non-oscillatory (WENO) scheme [11] was installed. As confirmation of this advection algorithm and as final confirmation of the metric derivatives of the transformation, solutions were obtained using the unmodified MM5 and using the transformed equations and adaptive algorithm. Overlay of the solution contours should provide confirmation of the Galilean invariance of the adaptive solution and of the metrics. As shown in Fig. 2, the adaptive procedure recovers the same solution as that of the fixed mesh except where the increased resolution of the adaptive mesh improves solution detail.

6. PROGRESS ON TURBULENCE MODELING

During this reporting period, the turbulence modeling was completed and runs were started. The k-ζ model has been expanded to include equations for the enthalpy variance

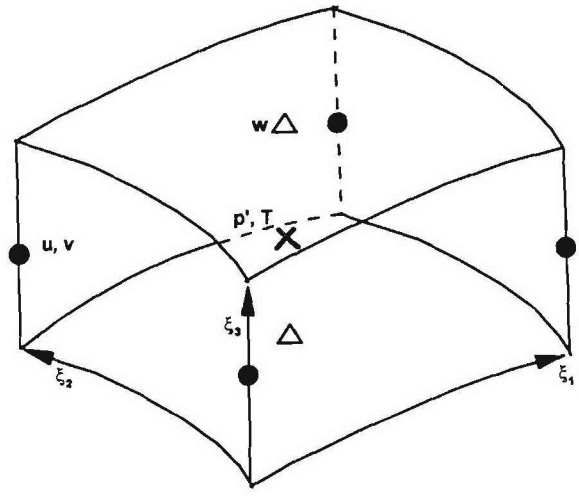

Figure 1. Arakawa B grid showing variable location.

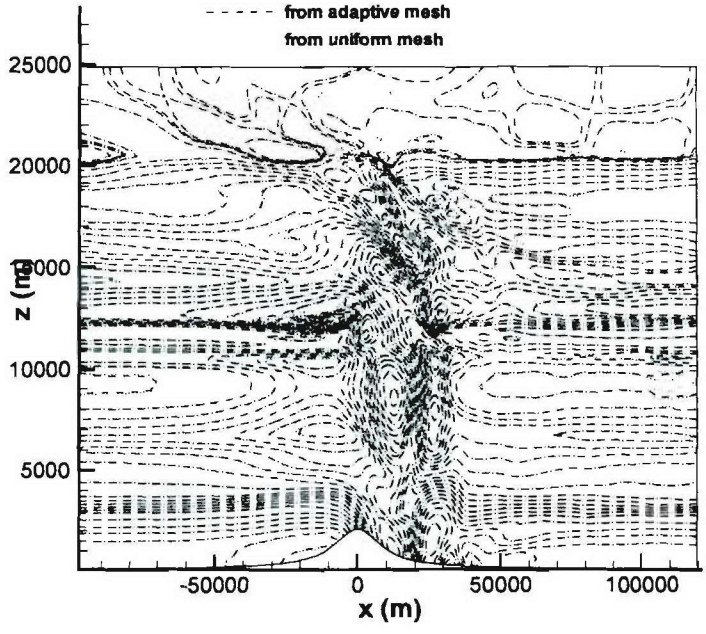

Figure 2. Comparison of potential temperature results (Colorado windstorm conditions [2]); dotted line: solution on the uniform mesh; dashed line: solution on the adaptive mesh after applying the WENO redistribution.

and its dissipation rate. The modeled equations are included in Appendix A in complete form.

A hybrid LES/RANS version of k-ζ model is given by

$$\frac{D(\bar{\rho}k)}{Dt} = \nabla \bullet \left[\left(\frac{\mu}{3} + \frac{\mu_t}{\sigma_k} \right) \nabla k \right] + \bar{\bar{\tau}} :: \bar{\bar{S}} - \frac{\mu_t}{\mathrm{Pr}_t} \frac{g}{\theta} \frac{\partial \theta}{\partial z} -$$

$$(1-\Gamma)\left(\frac{1}{C_k} \frac{\mu_t}{\bar{\rho}^2} \nabla \bar{\rho} \bullet \nabla \bar{P} + C_1 \frac{\bar{\rho}k}{\tau_\rho} + \mu\zeta\right) - \Gamma C_d \bar{\rho} \frac{k^{1.5}}{\Delta}$$

The blending function (Γ), that blends the LES and RANS and controls the regions where LES or RANS is dominant. In Ref. 9, the following blending was developed for wall-bounded flows:

$$\Gamma_\Delta = \tanh\left(\frac{l_\varepsilon}{\alpha_1 \Delta} \right)^2$$

$$l_\varepsilon = \frac{k^{\frac{1}{2}}}{\nu\zeta}$$

where Δ is the minimum mesh spacing, l_ε is the turbulence length scale, α_1 the model constant used to scale the influence of the minimum mesh size. Although this constant was originally modeled using aerodynamic flows, it did not function properly when used for atmospheric turbulence. The LES subgrid model has been used in the test cases in this report.

7. RESULTS AND DISCUSSION

7.1. 2-D Case

A two-dimensional case, based on an actual frontal event and subsequent windstorm downslope of the Colorado front range, is used to investigate the ability of DSAGA to resolve shear layers, gravity waves and their breakdown. This case is the same as that used in Reference 4 for evaluating the wave breaking prediction for various models by calculating the response to a generic mountain in the presence of an actual upwind sounding. For this 2-D case, the adaptive flow solver is executed on the full domain. The mountain profile is prescribed by a witch of Agnesi curve

$$z_s(x) = \frac{ha^2}{x^2 + a^2}$$

where h = 2 km is the mountain height and a = 10 km is the mountain half width, as shown in Figure 3. In order to compare with those results in Reference 4, the initial conditions are the same as theirs – horizontally homogeneous with the initial flow profile provided from the upstream sounding data of 11 January 1972, Grand Junction, Colorado, as shown in Figure 4. The same uniform grid is used to initialize the computation, which has 221 × 126 nodes with $\Delta z \approx 200$ m and $\Delta x \approx 1$ km. Free slip boundary conditions are applied to the lower boundary. Orlanski radiation boundary

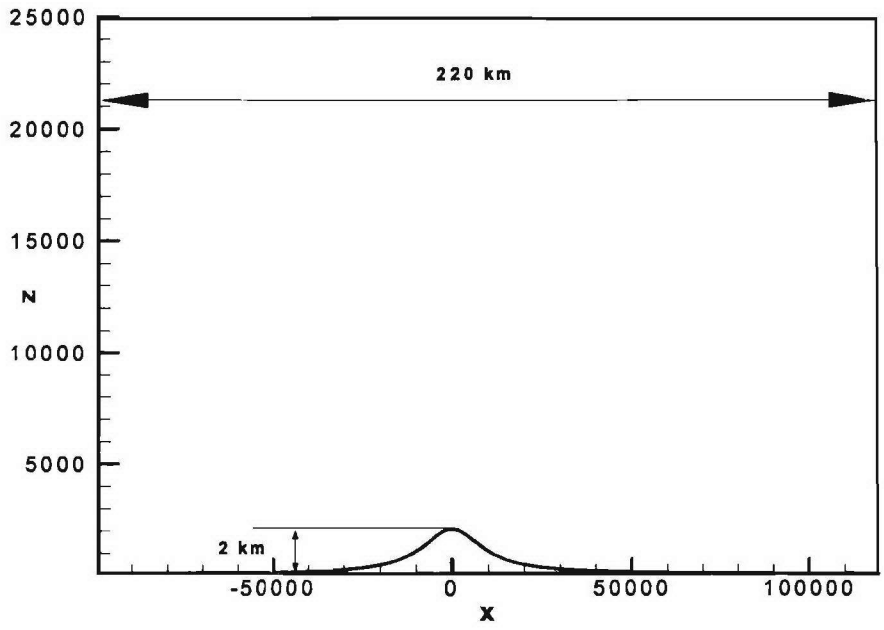

Figure 3. Geometry of the computational domain; mesh dimension 221X126.

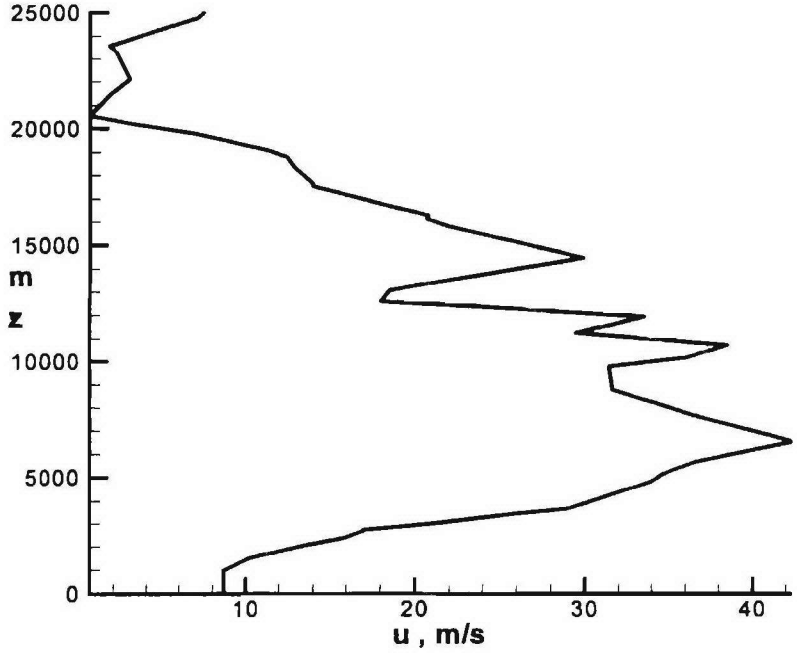

Figure 4. Velocity profile from the Grand Junction, CO, sounding for 1200 UTC, 11 January 1972

conditions [12] are applied to both inflow and outflow boundaries. A 5 km sponge layer is set at the top of the domain as a boundary condition to prevent the reflection of waves from the top boundary. A fourth order damping term is added to momentum and temperature equations to stabilize the flow solver.

In the following results, the grid adaptation is started from t = 0. The grid is preadapted from the uniform mesh by 100 adaptation cycles in order to resolve the initial flow field. The 4 grid adaptation cycles were performed after every 4 flow-solver iterations. One grid adaptation cycle is defined as the sequence of weight-function calculation, grid point relocation and solution redistribution. Two sets of results are obtained: one without turbulence modeling, the other with our hybrid RANS/LES model. For the former, the inherent numerical damping in the adaptive solver provides dissipation mechanism for turbulence, which can be considered as a Monotonically Integrated LES (MILES) simulation [13]. For the hybrid RANS/LES simulation, some tests showed that the hybrid scheme cannot switch from RANS to LES and turbulent kinetic energy (TKE). Figure 5 shows the potential temperature contours (θ), or the isotropes, for the MILES simulation at t = 5000 sec. Compared to the uniform mesh solution, the isotropes on the adaptive mesh clearly show the dynamic process of gravity wave overturning and break-down to turbulent eddies at $18 < z < 20$ km and $13 < z < 16$ km. Note that the breakdown is occurring in two distinct shear layers. The coherent turbulent structure at upper level atmosphere is essentially absent from the uniform mesh solutions because the 1 km mesh spacing is not able to resolve the 1.5 km long eddies at $z \approx 20$ km. As shown in Figure 6, the wave break-down is closely correlated with the regions of high vorticity (thus the choice of vorticity for the weight function). As a result of this, the grid nodes cluster around the wave breaking region and provide local resolution of $\Delta x \approx 300$ m and $\Delta z \approx 50$ m for resolving the small eddies. The potential temperature contours at t = 3 h for RANS/LES on the adaptive mesh are shown in Figure 7. The adaptive mesh at that moment is compared with the uniform mesh in Figure 8. Two bands of highly refined mesh at $z \approx 13$ km and 20 km above the mountain provide better resolution on small eddies within those regions. Another region of refined grid is aligned with the vortex street above the lee side of the mountain gives better resolution of lower-tropospheric eddies in front of the hydraulic jump. The third high resolution region is located on the top of the hydraulic jump due to a large size eddy located there. Figure 9 shows the contour of aircraft lift change response (to vertical gusts/velocity components), which can be used as an index to assess the turbulence level. The lift change is defined as:

$$\frac{\Delta L}{L} = \frac{V}{230(m/s)} C_{L\alpha}$$

where the $\Delta L / L$ is the relative change of lift, V the vertical velocity component and $C_{L\alpha} = 6$ is a lift coefficient. As can be seen from the $\Delta L / L$ contour, the lift change can be as large as 1 g, which has an adverse effect on aviation operation and safety in this region.

Figure 10 gives a profile of C_n^2 at x = 30 km, t = 3 h, which is calculated using Dewan's formula [14]. When compared to Figure 8, there is some correlation between

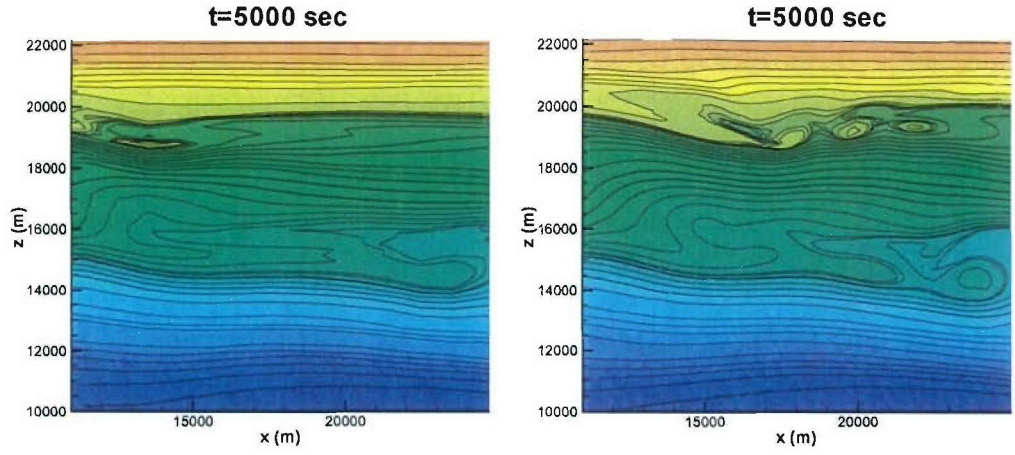

a) Fixed mesh b) Adapted mesh

Figure 5. Comparison of potential temperature contours on fixed and adapted mesh, LES-RANS.

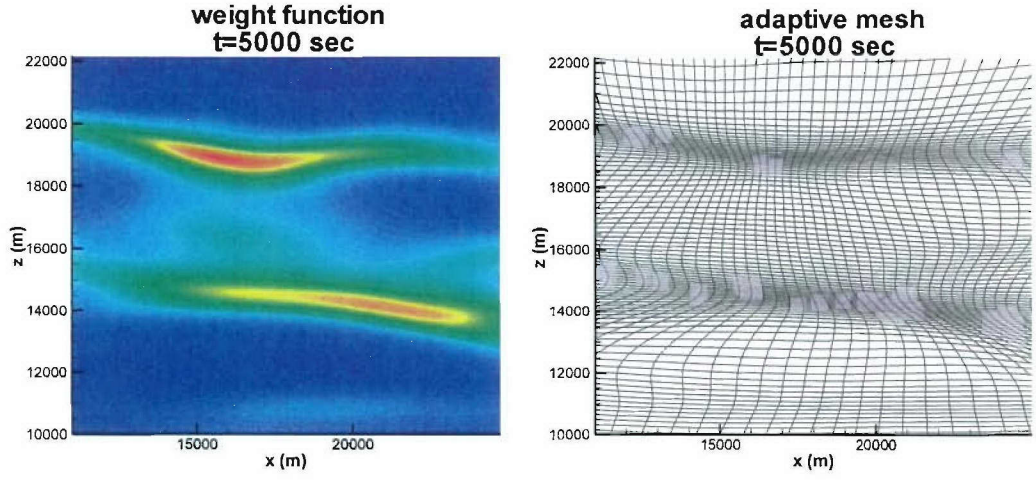

Figure 6. Typical response of adaptive mesh to weight function, LES-RANS.

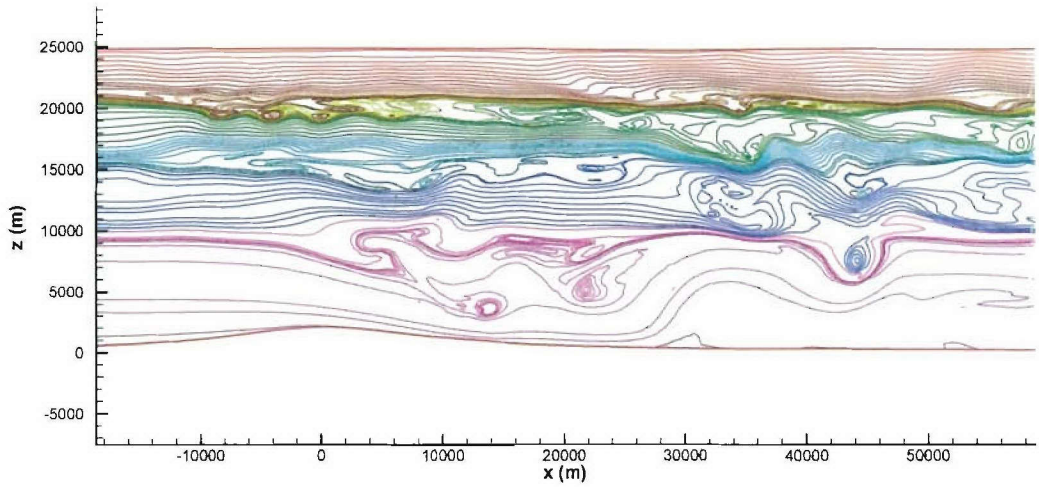

Figure 7. Potential temperature contours at t = 3 h.

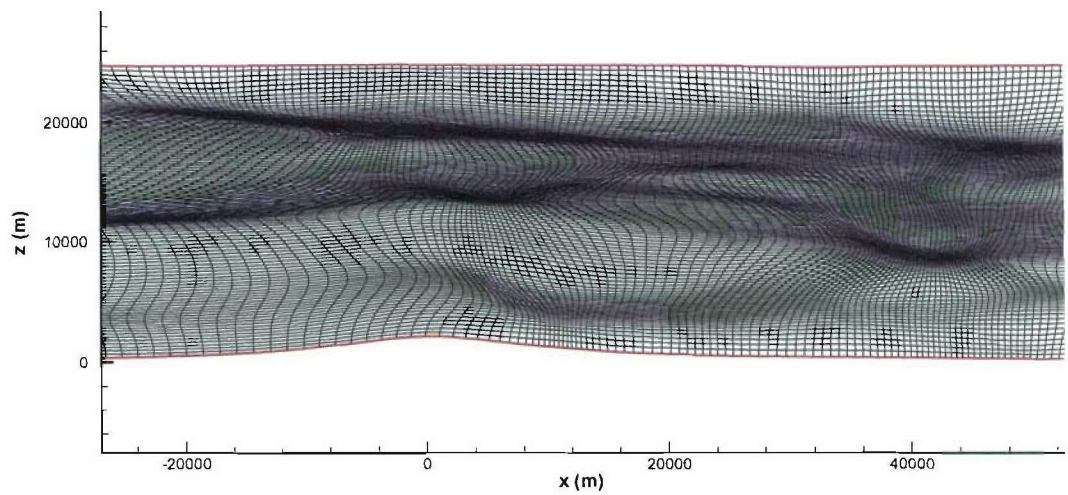

Figure 8. Detail of adapted computational mesh at the t=3 h solution time.

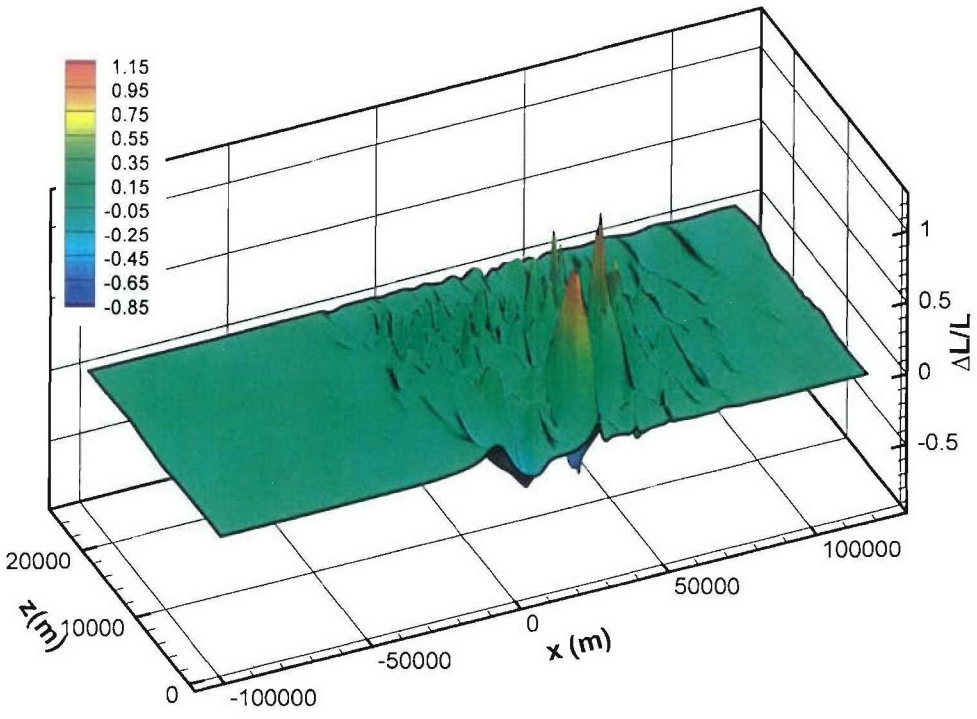

Figure 9. Lift change ($\Delta L / L$) contours

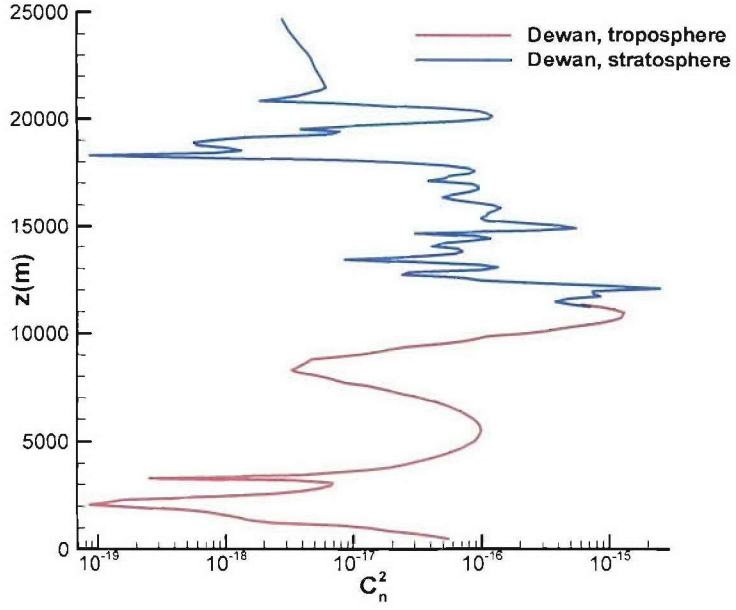

Figure 10. C_n^2 profile at x = 30 km, t = 3 h.

high C_n^2 regions and refined mesh regions. Therefore, these high C_n^2 regions are due mainly to high shear and wave-breaking.

7.2. 3-D Case

In this case, the adaptive algorithm is integrated into MM5 code to simulate the SOC (Storm of the Century) case, a tutorial case for MM5. Figure 11 presents the layout of the two-level nested grid for this simulation with MM5 36employed in both levels. Its solution in level 2 provides the boundary conditions for the current adaptive flow solver. The initial grid for the adaptive solver is the same as the level 2 grid with 49×52×23 nodes. For this case, all Planetary Boundary Layer options in MM5 are turned off and the free slip boundary condition is used. The MILES scheme is used in the imbedded region. To advance the solution to the same level as the outer MM5 solution, the time step in the imbedded adaptive mesh is determined by:

$$\Delta t = \Delta t_{MM5} / \text{nint}(\frac{\Delta t_{MM5}}{\min(\Delta t_{loc})} + 0.5)$$

where Δt_{MM5} is the time step on the outer MM5 domain, Δt_{loc} is the local time step, nint is a Fortran function for nearest integer. Figure 12 shows the evolution of the grid in a ξ_1 = const plane. The contours for the magnitude of vorticity are also shown in the same figure. As can be seen from the grid node distribution, the high shear layers near the surface and in the upper atmosphere are dynamically captured, i.e., the high resolution grid always adapts to the region with large vorticity (shear) and moves with it. Figure 13 shows the grid and contours in ξ_3 = const plane next to the surface. Again, the high vorticity region is well resolved. The minimum mesh spacing in the region shown in Figure 13 is about 6 km, which is about one fifth of the initial mesh spacing (30 km). These two figures clearly demonstrate that the current algorithm can resolve high velocity gradients in both vertical and horizontal directions.

8. CONCLUSIONS

Significant progress was made during this reporting period towards the ultimate goal of a fully functioning mesoscale model for predicting the likelihood of optical turbulence under specified conditions and topography. Incorporation of the k-ζ turbulence model into the entire modeling system was completed and checkout of the model blending algorithm indicates some differences in scale as might be expected. Reproduction of the fixed mesh results by the adaptive mesh algorithm was confirmed. The results show that the vorticity is a good indicator for gravity wave-breaking. The entire wave-breaking process in the 2-D case is well-captured and resolved in adaptive mesh.

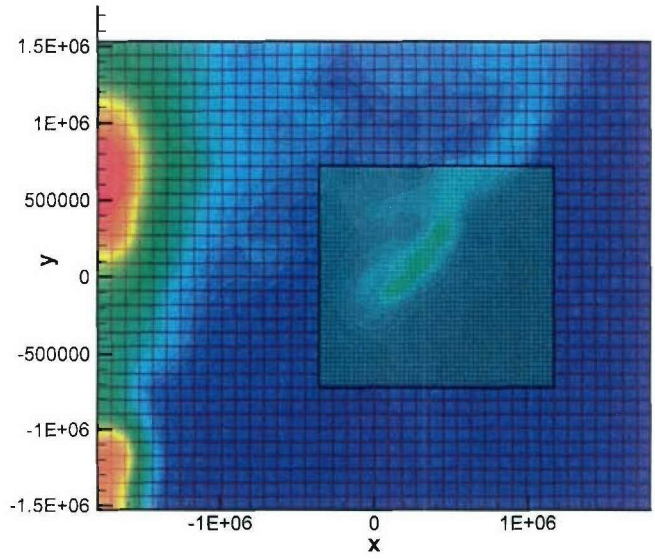

Figure 11. The layout of two-level nested grid and terrain contours.

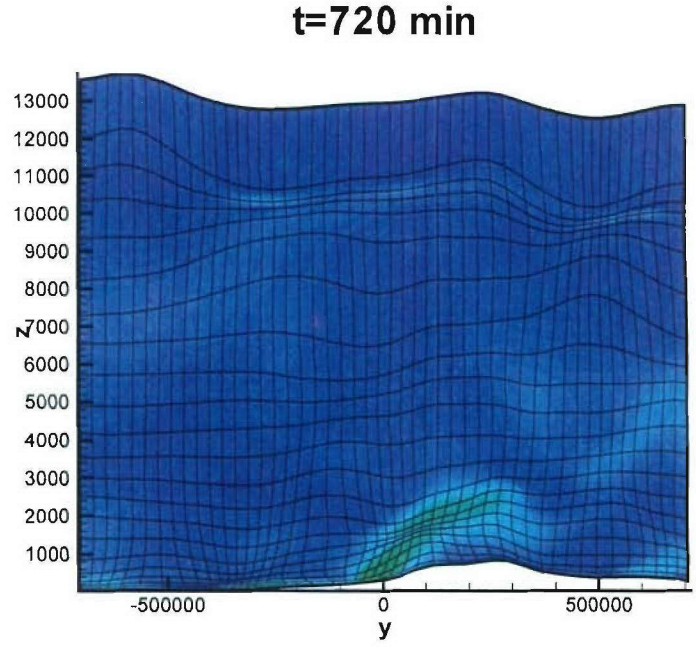

Figure 12. Grid and the vorticity magnitude contours in ξ_1 = const. surface.

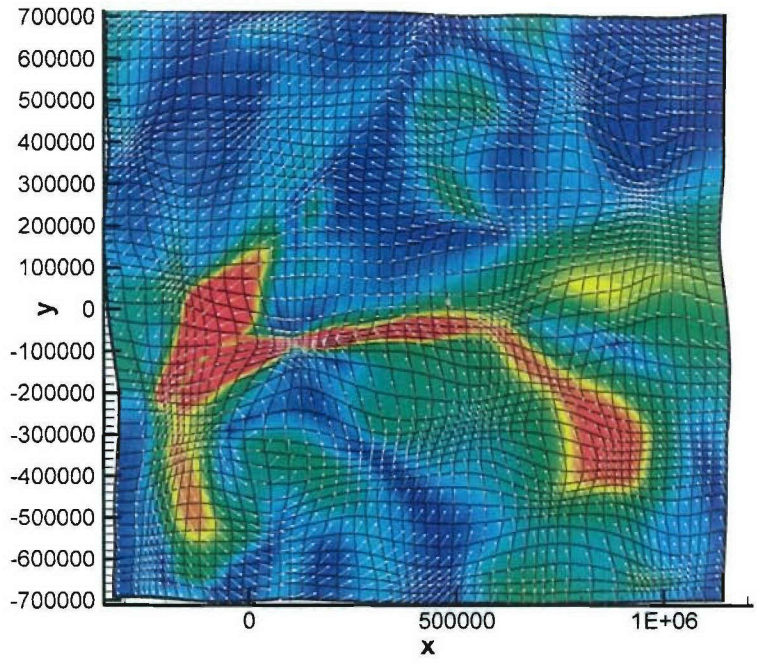

Figure 13. The vorticity magnitude contours and horizontal velocity vectors in ξ_3 = const plane at t = 720 min.

REFERENCES

1. Fritts, D. C. and Alexander, M., "GravityWave Dynamics and Effects in the Middle Atmosphere," Reviews of Geophysics, Vol. 41, No. 1, 2003, pp. 1–64.
2. Jumper, G. Y. and Beland, R. R., "Progress in the Understanding and Modeling of Atmospheric Optical Turbulence," AIAA Paper 2000-2355, 2000.
3. Grell, G. A., Dudhia, J., and Stauffer, D. R., "A Description of the Fifth-Generation Penn State/NCAR Mesoscale Model (MM5)," NCAR TECHNICAL NOTE NCAR/TN–398+STR, June 1995.
4. Doyle, J. D., Durran, D., Chen, C., Collie, B. A., Georgelin, M., Grubisic, V., Hsu, W. R., Huang, C. Y., Landau, D., Lin, Y. L., Poulos, G. S., Sun, W. Y., Webber, D. B., Wurtele, M. G., and Xue, M., "An Intercomparison of Model-Predicted Wave Breaking for the 11 January 1972 Boulder Windstorm," Monthly Weather Review, Vol. 128, No. 3, 2000.
5. Laflin, K. R. and McRae, D. S., "Solution-Dependent Grid-Quality Assessment and Enhancement," Proceedings: 5th International Conference on Numerical Grid Generation in Computational Field Simulations, April 1–5, 1996, pp. 3–12.
6. Laflin, K. R., Solver-independent r-refinement adaptation for dynamic numerical simulations, Ph.D. diss., North Carolina State University, Raleigh, NC, 1997.
7. McRae, D. and Laflin, K., "Dynamic Grid Adaption and Grid Quality," Handbook of Grid Generation, edited by J. F. Thompson, B. K. Soni, and N. P. Wetherill, CRC Press,Boca Raton, 1999, pp. 34–1 to 34–33.
8. Robinson, D. F., Harris, J. E., and Hassan, H. A., "Unified Turbulence Closure Model for Axisymmetric and Planar Free Shear Flows," AIAA Journal , Vol. 33, No. 12, 1995, pp. 2325–2331.
9. Xiao, X., Edwards, J. R., Hassan, H. A., and Baurle, R. A., "Inflow Boundary Conditions for Hybrid Large Eddy/Reynolds Averaged Navier-Stokes Simulation," AIAA Journal , Vol. 41, No. 8, August 2004, pp. 1481–1489.
10. Arakawa, A. and Lamb, V. R., "Computational design of the basic dynamical processes of the UCLA general circulation model," Methods in Compu. Phys., Vol. 17, pp. 173–265.
11. Shu, C.-W., "Essential Non-Osclllatory and Weighted Essentially Non-Oscillatory Schemes for Hyperbolic Conservation Laws," ICASE Report 97-65, 1997, NASA/CR-97-206253.
12. Orlanski, I., "A simple Boundary Condition for Unbounded Hyperbolic Flows," Journal of Computational Physics, Vol. 21, 1976, pp. 251–269.
13. Boris, J. P., Grinstein, F. F., Oran, E. S., and Kolbe, R. J., "New Insights into large Eddy Simulation," Fluid Dynamics Research, Vol. 10, No. 4-6, 1992, pp. 65–90.
14. Dewan, E. M., Good, R. E., Beland, R., and Brown, J, "A Model for C_n^2 (Optical Turbulence) Profiles using Radiosonde Data", Environmental Research Papers, PL-RT-93-2043, AD-A279399, Phillips Laboratory, 1993.

Appendix.

Turbulence Model Equations

k equation:

$$\frac{\partial}{\partial t}(\bar{\rho}k)+\frac{\partial}{\partial x_j}\left(\bar{\rho}\bar{u}_j k\right)=\frac{\partial}{\partial x_j}\left[\left(\frac{\mu}{3}+\frac{\mu_t}{\sigma_k}\right)\frac{\partial k}{\partial x_j}\right] + \tau_{ij}\frac{\partial \bar{u}_i}{\partial x_j}-\frac{1}{C_k}\frac{\mu_t}{\bar{\rho}^2}\frac{\partial \bar{\rho}}{\partial x_i}\frac{\partial \bar{P}}{\partial x_i}-C_1\frac{\bar{\rho}k}{\tau_\rho}-\mu\zeta + \frac{\bar{\rho}}{\theta}\left[g\,\delta_{i3}+2\Omega_0\in_{ijk}\eta_j\,\tilde{u}_k\right]\overline{\theta'' u_i''} \qquad (A.1)$$

ζ-equation:

$$\frac{\partial}{\partial t}(\bar{\rho}\zeta)+\frac{\partial}{\partial x_j}(\bar{\rho}\bar{u}_j\zeta)=\frac{\partial}{\partial x_j}\left[\left(\mu+\frac{\mu_t}{\sigma_\zeta}\right)\frac{\partial \zeta}{\partial x_j}\right] + \frac{\mu_t}{\sigma_r}\frac{\partial \Omega_i}{\partial x_j}\left(\frac{\partial \Omega_i}{\partial x_i}+\frac{\partial \Omega_j}{\partial x_i}\right)-\varepsilon_{mij}\frac{\partial \Omega_i}{\partial x_j}\left[\frac{\partial}{\partial x_l}(u_m'' u_l'')-\frac{\partial k}{\partial x_m}\right] - \frac{2\beta_6\tau_{ij}\nu_t}{k\nu}\Omega\Omega_i\Omega_j+\frac{\beta_7\bar{\rho}\zeta}{\Omega^2}\Omega_i\Omega_j\bar{s}_{ij}+2\beta_8\varepsilon_{ilm}\left(\frac{\tau_{ij}}{k}\right)\frac{\partial k}{\partial x_l} + \left(\alpha_3 b_{ij}+\frac{1}{3}\delta_{ij}\right)\bar{\rho}\zeta\bar{s}_{ij}-\frac{\beta_4\bar{\rho}\tau_{ij}\Omega_i\Omega_j}{k\Omega}-\frac{\beta_5}{R_k+\delta}\bar{\rho}\zeta^{\frac{3}{2}} \times\frac{\partial \zeta}{\partial x_m}\frac{\Omega_j}{(\bar{s}^2+\Omega^2/2)}+\max[P_\zeta,0]-2\bar{\rho}\zeta\bar{s}_{ii}-C_{\zeta 1}\frac{\mu_t\zeta\Omega}{\tau_\rho k} - C_{\zeta,1}\,g\,\delta_{i3}\in_{lmi}\Omega_{lm}\sqrt{\left(\frac{\partial \rho}{\partial x_i}\right)^2}+C_{\zeta,2}\,\Omega\,\eta_j\sqrt{k}\frac{\partial \tilde{u}_l}{\partial x_j}\frac{\partial \bar{\rho}}{\partial x_l} + 2\Omega_0 C_{\zeta,3}\,\bar{\rho}\,\eta_j\,\Omega_j\,\zeta^{1/2};\quad \Omega^2=\Omega_i\,\Omega_i \qquad (A.2)$$

Enthalpy Variance Equation:

$$\frac{\partial(\bar{\rho}h''^2/2}{\partial t}+\frac{\partial(\bar{\rho}\tilde{u}_j h''^2/2)}{\partial x_j}=\frac{\partial}{\partial x_j}\left[\bar{\rho}\left(\alpha+\frac{\alpha_t}{C_{h,2}}\right)\frac{\partial(h''^2/2)}{\partial x_j}\right] - q_{t,j}\frac{\partial \tilde{h}}{\partial x_j}-\bar{\rho}\in_h+4\mu\tilde{S}_{ij}\left[\left(\alpha_t+\frac{\nu_t}{C_{h,3}}\right)\frac{\partial^2\tilde{h}}{\partial x_i\partial x_j}\right] - \frac{4}{3}\mu\tilde{S}_{ij}\left[\left(\alpha_t+\frac{\nu_t}{C_{h,3}}\right)\frac{\partial^2\tilde{h}}{\partial x_i^2}\right]+2\mu C_{h,4}\sqrt{h''^2\zeta} \qquad (A.3)$$

where

$$q_{t,j} = -\bar{\rho}\alpha_t \frac{\partial \tilde{h}}{\partial x_j} + \bar{\rho}\,\tau_h\, g\,\delta_{i3}\sqrt{h''^2}$$

$$\alpha_t = \frac{1}{2}\left(C_h k \tau_h + \nu_t / 0.89\right)$$

$$\tau_h = h''^2 / \epsilon_h$$

$$\epsilon_h = \alpha\overline{\left(\frac{\partial h''}{\partial x_j}\right)^2}$$

Dissipation Rate Equation for Enthalpy Variance:

$$\frac{\partial \bar{\rho}\,\epsilon_t}{\partial t} + \frac{\partial \bar{\rho}\tilde{u}_j\,\epsilon_h}{\partial x_j} = \frac{\partial}{\partial x_j}\left[\left(\bar{\rho}\alpha + \frac{\mu_t}{C_{h,7}}\right)\frac{\partial \epsilon_h}{\partial x_j}\right]$$
$$- C_{h,5}\bar{\rho}\,\epsilon_h\left(b_{jk} + \frac{\delta_{jk}}{3}\right)\frac{\partial \tilde{u}_j}{\partial x_k} + \frac{\bar{\rho}k}{C_{h,6}}\frac{\partial\sqrt{h''^2}}{\partial x_j}\frac{\partial \tilde{h}}{\partial x_j}$$
$$- \frac{q_{t,j}}{C_{h,8}\tau_h}\frac{\partial h}{\partial x_j} + \frac{\alpha\mu_t}{C_{h,3}}\left(\frac{\partial^2 \tilde{h}}{\partial x_i \partial x_j}\right)^2 \qquad \text{(A.4)}$$

where

$$b_{jk} = \frac{\tau_{jk}}{\bar{\rho}k} + \frac{2}{3}\delta_{jk}$$